mater.scichina.com link.springer.com Published online 20 March 2023 | https://doi.org/10.1007/s40843-022-2370-1

Encapsulating Si nanoparticles in multi-shell hollow spheres: An effective approach to boost the cyclability

Huan Du[1,2], Ruohan Yu[2,3], Xingnian Tan[1], Jinsong Wu[1,3], Dongyuan Zhao[1], Liqiang Mai[1,4] and Liang Zhou[1,4*]

ABSTRACT Silicon is an appealing lithium-ion battery anode material; unfortunately, it is confronted with unsatisfactory cyclability owing to its large volume change. Herein, we design a unique ternary composite anode material ($Si/Cr_2O_3/C$), where the Si nanoparticles are confined in carbon-coated chromium oxide multi-shell hollow spheres (MSHSs). Encapsulating the Si nanoparticles in the MSHSs effectively boosts the cyclability owing to the available free space for volume change buffering and the ideal structural stability of the Cr_2O_3/C hybrid matrix. The rationally designed $Si/Cr_2O_3/C$ ternary composite demonstrates not only high reversible capacity (1351 mA h g^{-1} at 100 mA g^{-1}) but also stable cycling (716 mA h g^{-1} after 300 cycles at 500 mA g^{-1}). This contribution proposes a novel multi-shell hollow structure design to solve the poor cyclability problem of Si-based anode materials.

Keywords: multi-shell hollow structure, silicon, anode material, encapsulation, chromium oxide

INTRODUCTION

The development of lithium-ion batteries (LIBs) with high energy density and satisfactory cyclability is of essential significance to satisfy the ever-increasing needs for electrical vehicles [1–3]. The anode material calls for revolution as the current commercial material, graphite, shows a relatively low theoretical capacity [4,5]. Therefore, exploring novel anode materials with high capacity and desirable working potential has been put into a foremost position.

Elemental Si is an alternative LIB anode material due to its incomparable theoretical gravimetric capacity (≈4200 mA h g^{-1}) [6–8]. Nevertheless, bare Si suffers from particle pulverization, unstable solid electrolyte interphase (SEI), and unsatisfactory cyclability, which originate from the large volume change (≈ 400%) during cycling [9,10]. The rational structural design represents an effective approach to tackle the above-mentioned challenges of Si. Various Si-based nanostructures, including nanowires [11], nanotubes [12], mesoporous structure [13], core-shell design [14], yolk-shell spheres [15], hierarchical structure [16], and pomegranate structure [17], have been constructed to boost the electrochemical performances. Multi-shell hollow structure featuring concentric separated shells has demonstrated multiple advantages in energy storage [18–21]. This unique structure could provide not only sufficient free space to buffer the volume variations of active components, but also reduced paths for solid-state ion transfer, which is beneficial for cyclability and rate capability. However, the composition of multi-shell hollow structures is usually limited to metal oxides, metal sulfides, silica, and carbon [22,23]. To our knowledge, there are rare reports on elemental Si-based multi-shell hollow structures, although such materials [24,25] would be very appealing for lithium storage. In addition, the encapsulation of Si nanoparticles into multi-shell hollow structures is quite challenging as the synthesis of such intricate structures is usually tedious and requires delicate control on synthetic conditions.

Herein, we report a facile spray drying approach to produce a $Si/Cr_2O_3/C$ ternary composite anode material, in which Si nanoparticles are confined in carbon-coated Cr_2O_3 multi-shell hollow spheres (MSHSs). The Si nanoparticles offer a high capacity; the multi-shell hollow structure provides efficient paths for the electrolyte to access the Si nanoparticles and enough space to buffer the volume swelling of Si; Cr_2O_3 helps stabilize the multi-shell hollow structure and contributes to a certain capacity; the amorphous carbon coatings not only enhance the conductivity but also contribute to the structural stability of the composite. The rational structural design endows the $Si/Cr_2O_3/C$ hybrid a stable high-capacity of 1007 mA h g^{-1} after 100 cycles at 100 mA g^{-1}.

EXPERIMENTAL SECTION

Material synthesis

In a typical synthesis, 10 mmol chromium(III) nitrate nonahydrate ($Cr(NO_3)_3{\cdot}9H_2O$), 10 mmol sucrose, and 10.7 mmol Si nanoparticles (~0.3 g) were dispersed in 150 mL water and adequately stirred. Afterward, the suspension was spray dried employing a B-290 Buchi mini spray dryer. The detailed conditions for spray drying were listed as follows: inlet temperature of 220°C, aspirator rate of 90%, rotameter setting of 40 mm, and pump rate of 5%. The Si/Cr_2O_3 MSHSs were acquired after annealing the obtained powder at 400°C for 4 h in air. The $Si/Cr_2O_3/C$ MSHSs were obtained after annealing the Si/Cr_2O_3

[1] State Key Laboratory of Advanced Technology for Materials Synthesis and Processing, Wuhan University of Technology, Wuhan 430070, China
[2] International School of Materials Science and Engineering, Wuhan University of Technology, Wuhan 430070, China
[3] Nanostructure Research Center (NRC), Wuhan University of Technology, Wuhan 430070, China
[4] Hubei Longzhong Laboratory (LZL), Wuhan University of Technoology, Xiangyang 441106, China
* Corresponding author (email: liangzhou@whut.edu.cn)

MSHSs at 800°C in flowing C_2H_2/Ar (5%/95%, 200 mL min^{-1}) for 0.5 h.

Materials characterizations

Scanning electron microscopy (SEM) images were collected on a JEOL-7100F field emission SEM, while transmission electron microscopy (TEM), high-resolution TEM (HRTEM), and high-angle annular dark-field scanning TEM (HAADF-STEM) images were obtained on a JEM-2100F and Titan Themis^3 G2 300. X-ray diffraction (XRD) analysis was carried out on a Bruker D8 Discover X-ray diffractometer with a Cu Kα X-ray source (λ = 1.5418 Å). Raman spectra were recorded on a Renishaw INVIA Raman microscope with a 532-nm laser. Thermogravimetric analysis (TGA) was acquired *via* an STA-449C thermobalance with a heating rate of 5°C min^{-1} in air. X-ray photoelectron spectroscopy (XPS) characterizations were performed on a VG Multilab 2000 with an Al Kα monochromated X-ray source. Fourier-transform infrared (FT-IR) spectra were obtained on a Nicolet 6700 IR spectrometer.

Electrochemical measurement

The working electrodes consisted of active materials (70 wt%), acetylene black (20 wt%), and sodium alginate (10 wt%) coated on Cu foil. The coin-type half-cells (CR2016) were assembled in an Ar-filled glove box. $LiPF_6$ (1.0 mol L^{-1}) in ethylene carbonate/dimethyl carbonate (1:1 in volume) with 10 vol% fluoroethylene carbonate (FEC) was used as the electrolyte. Si/Cr_2O_3/C//$LiFePO_4$ full-cells were also assembled. Si/Cr_2O_3/C was first cycled in half-cells for several cycles and then taken out for full-cell assembly. The $LiFePO_4$ cathodes were composed of $LiFePO_4$, super-P, and poly(vinylidenefluoride) (PVDF) with a mass ratio of 7:2:1 on an Al foil.

Galvanostatic charge-discharge (GCD) measurements (0.01–1.5 V *vs.* Li^+/Li) were performed on a LAND CT2001A multichannel battery testing system. Cyclic voltammetry (CV) profiles were obtained on a PGSTAT 302N workstation at a scan rate of 0.1 mV s^{-1}. Electrochemical impedance spectroscopy (EIS) curves were collected at a frequency range of 0.01 Hz to 100 kHz with a potential amplitude of 10 mV.

In-situ characterizations

The electrodes for *in-situ* XRD and Raman studies were composed of active materials (70 wt%), acetylene black (20 wt%), and polytetrafluoroethylene (PTFE, 10 wt%). *In-situ* XRD experiments were performed on a D8 Discover X-ray diffractometer equipped with a planar detector. The anode was placed on the back side of an X-ray transparent Be window which also served as the current collector. The *in-situ* XRD signals were collected in the range of 25°–42° with a still mode. Each pattern was acquired in 120 s. *In-situ* Raman experiments were performed on a Renishaw INVIA Raman microscope. The anode was placed on the back side of the sapphire window with titanium foil as the current collector. The *in-situ* Raman spectra were collected in the range of 50–2000 cm^{-1} with a still mode. Each pattern was acquired in 120 s.

RESULTS AND DISCUSSIONS

The construction of Si/Cr_2O_3/C MSHSs generally involves three steps (Fig. 1a), including spray drying, annealing in air, and chemical vapor deposition (CVD). In the first step, an aqueous suspension containing $Cr(NO_3)_3{\cdot}9H_2O$, sucrose, and Si nanoparticles (~50 nm, Fig. S1) is spray dried into microspheres using a two-fluid nozzle. The obtained Si/$Cr(NO_3)_3$/sucrose composite is annealed in air, during which the temperature gradient-induced heterogeneous contraction occurs and results in the formation of a multi-shell hollow structure [26–28]. In detail, the temperature exerted on the surface of Si/$Cr(NO_3)_3$/sucrose intermediate spheres is higher than that exerted on the core. Such a temperature gradient facilitates the surface decomposition into a Cr_2O_3 shell, leaving the core unchanged. As the Cr_2O_3 shell is rigid while the core continues to decompose, contract, and detach from the shell during heat treatment, Si/Cr_2O_3 MSHSs eventually form. During the final CVD process in flowing C_2H_2/Ar, C_2H_2 penetrates the porous Cr_2O_3 shells and amorphous carbon coatings are deposited, leading to the formation of Si/Cr_2O_3/C MSHSs [29]. Cr_2O_3 was selected as the matrix to confine the Si nanoparticles as it is a potential anode material for both lithium- and sodium-ion batteries with relatively low working potential and high ionic conductivity [30,31].

The microstructure of Si/Cr_2O_3/C was first studied by SEM and TEM. Si/Cr_2O_3/C manifests a microsphere morphology with a size ranging from 400 to 4000 nm (Fig. S2a). Under a high magnification, the nanoparticulate and nanoporous characteristics of Si/Cr_2O_3/C can be clearly discovered (Fig. 1b). From the broken part of a typical microsphere, an inner core is exposed, demonstrating the MSHS structure (Fig. S2b). Conventional TEM image confirms that Si/Cr_2O_3/C possesses MSHS structure (Fig. 1c) and each microsphere contains three to four nanoparticulate shells. In the HRTEM images, the (311) lattice fringes of Si (Fig. 1d) and (012) lattice fringes of Cr_2O_3 (Fig. 1e) are observed. Besides, a uniform and thin carbon coating layer with a thickness of ~5 nm can be easily found on the surface of nanoparticle building blocks (Fig. 1f). Selected area electron diffraction (SAED) pattern exhibits a series of concentric rings, which can be assigned to the (111), (220), and (311) diffractions of Si nanoparticles, as well as (012), (104), (110), (113), and (300) diffractions of Cr_2O_3 (Fig. 1g).

HAADF-STEM and energy dispersive spectroscopy (EDS) mappings were conducted on different particles to reveal the distribution of Si nanoparticles and C in the composite. The HAADF-STEM image of an individual Si/Cr_2O_3/C microsphere manifests a contrast between darker regions and lighter periphery, further demonstrating the MSHS structure (Fig. 1h). Low magnification mappings show the uniform distribution of Cr, O, Si, and C elements in the Si/Cr_2O_3/C composite (Fig. 1i and Fig. S3). The overlapping of Si and Cr signals suggests the successful encapsulation of Si nanoparticles in the multi-layered shells. The observation of C signal on each shell indicates the successful deposition of acetylene-derived carbon on the shells. This is due to the porous feature of Si-Cr_2O_3 and small molecular size of acetylene (< 0.5 nm) [32].

For comparison, a series of samples with different Si contents were prepared. Without Si nanoparticles, Cr_2O_3 and Cr_2O_3/C manifest a well-defined MSHS structure (Fig. S4). For the Cr_2O_3/C composite microspheres, no signal for Si can be detected in the mappings as expected (Fig. S5). With the introduction of a small amount Si nanoparticles (0.1–0.3 g), the MSHS structure can be generally retained while the surface roughens (Table S1 and Fig. S4). When an excess amount of Si nanoparticles is added (0.4 g), more broken spheres form (Fig. S4).

XRD patterns of the Si/Cr_2O_3/C, Si/Cr_2O_3, and Cr_2O_3/C are

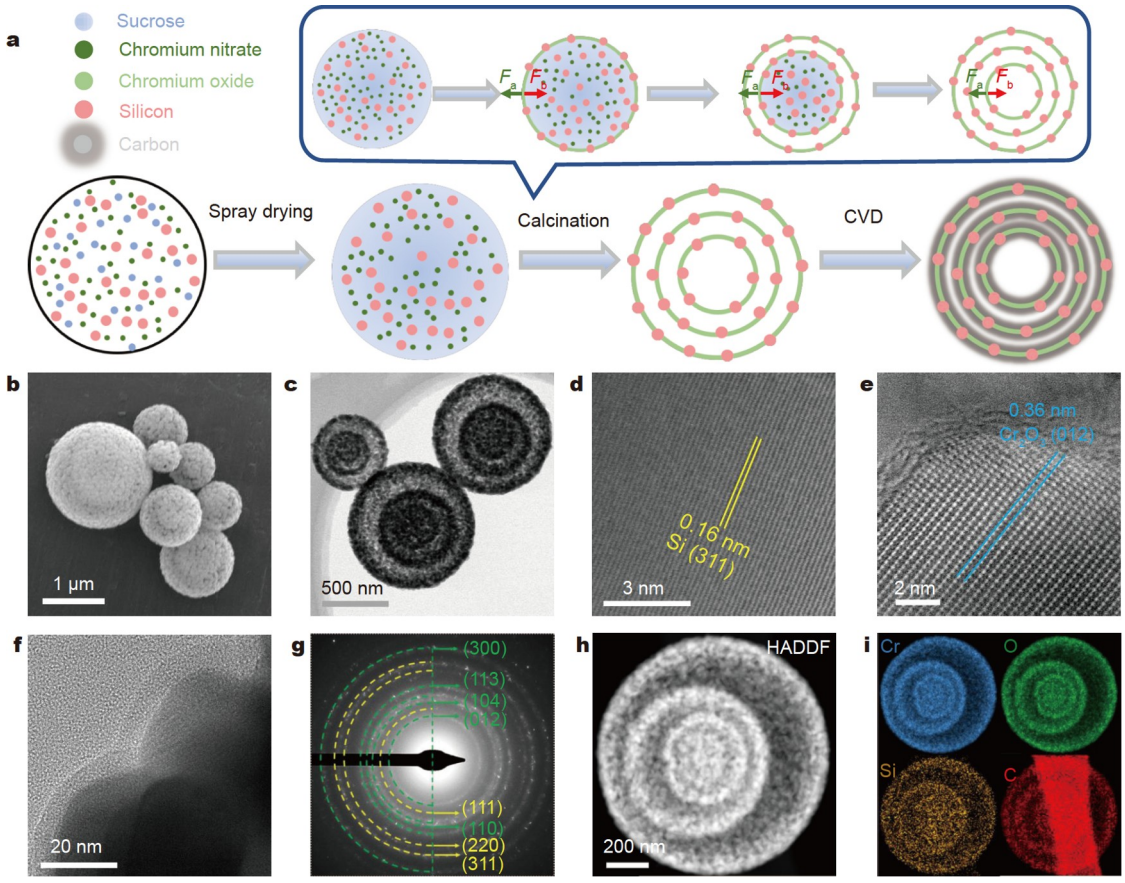

Figure 1 Synthesis scheme and microstructure characterizations. (a) Schematic illustration for the construction of Si/Cr_2O_3/C MSHSs; (b) SEM image, (c) TEM image, (d, e) HRTEM images, (f) TEM image, (g) SAED pattern, (h) HAADF-STEM image, and (i) elemental mappings of Si/Cr_2O_3/C.

presented in Fig. 2a and Fig. S6. All of the synthesized samples present diffraction peaks at 24.5°, 33.6°, 36.2°, 41.5°, 50.2°, 54.9°, 63.4°, and 65.1°, which are characteristic peaks for Cr_2O_3. Si/Cr_2O_3/C and Si/Cr_2O_3 display additional peaks from crystalline Si at 28.4°, 47.3°, and 56.1°. The crystallite size of Cr_2O_3 is calculated to be ~25 nm (Table S2) by applying the Scherrer equation to the strongest diffraction peaks, which is also consistent with the particle size in TEM (Fig. S7). There is no obvious diffraction peak for C in Si/Cr_2O_3/C and Cr_2O_3/C, which can be ascribed to the almost amorphous characteristic of C. Si/Cr_2O_3/C and Si/Cr_2O_3 display a sharp band at ~520 cm^{-1} in the Raman spectra, in accordance with the strong Si–Si stretching. Si/Cr_2O_3/C and Cr_2O_3/C exhibit broad D bands (1353 cm^{-1}) and G bands (1602 cm^{-1}) (Fig. 2b and Fig. S8). The D and G bands have similar intensities, confirming the amorphous carbon coating layers. Cr_2O_3/C displays a weak peak at ~558 cm^{-1}, representing Cr–O lattice vibrations. TGA was employed to determine the carbon content of Si/Cr_2O_3/C (Fig. 2c). The combustion of amorphous carbon causes an evident weight loss of 6.5 wt% at ~400–600°C. With increasing temperature, Si/Cr_2O_3/C shows a weight gain above 800°C, resulting from the oxidation of Si to SiO_x. According to the feeding ratio, the contents of Si and Cr_2O_3 are calculated to be 26.5 and 67 wt%, respectively.

XPS affords valuable information on the surface composition and valence states. Before testing, Ar^+ etching was conducted for Si/Cr_2O_3/C in consideration of the shallow effective detecting depth (less than 10 nm) [33]. The survey spectrum of Si/Cr_2O_3/C verifies the existence of Si, Cr, O, and C in the sample (Fig. S9a). The C 1s spectrum of Si/Cr_2O_3/C can be fitted into sp^2-bonded C, C–O, and C=O bonds (Fig. S9b). The core-level Si 2p spectra (Fig. 2d–f) of Si, Si/Cr_2O_3, and Si/Cr_2O_3/C all contain four components: Si^0 (98.9 eV), Si^+ (99.9 eV), Si^{2+} (101.9 eV), and Si^{3+} (102.9 eV) [34]. As expected, the surface of Si nanoparticles is dominated by Si^0. For Si/Cr_2O_3 and Si/Cr_2O_3/C, the Si^{2+} species increases sharply owing to the inevitable oxidation during calcination. The O 1s spectrum of Cr_2O_3/C can be deconvoluted into C–O–C and Cr–O bonds (Fig. S9c). After Si encapsulation, additional peaks from Si–O–Si and Si–O–C can be observed. The observation of Si–O–C covalent bond demonstrates the strong interaction between Si particles and Cr_2O_3/C matrices (Fig. S9c). The Cr 2p spectrum contains two peaks at 576.8 and 586.4 eV, which are assigned to Cr $2p_{3/2}$ and $2p_{1/2}$ components, respectively (Fig. S9d) [35]. The functional groups on Si/Cr_2O_3/C were further analyzed by FT-IR, where the Si–O–C, Cr–O, and C=C groups can be identified, further proving the covalent interaction between Si nanoparticles and Cr_2O_3/C hosts (Fig. S10).

CV profiles of the Si/Cr_2O_3/C are recorded in Fig. 3a to study the lithiation/de-lithiation processes. For the initial cathodic process, the peak at 1.07 V is from the generation of an SEI film owing to the decomposition of FEC-containing electrolytes. This wide peak disappears in the second cycle, which proves the good stability of the SEI film. The cathodic peak at 0.01 V is assigned

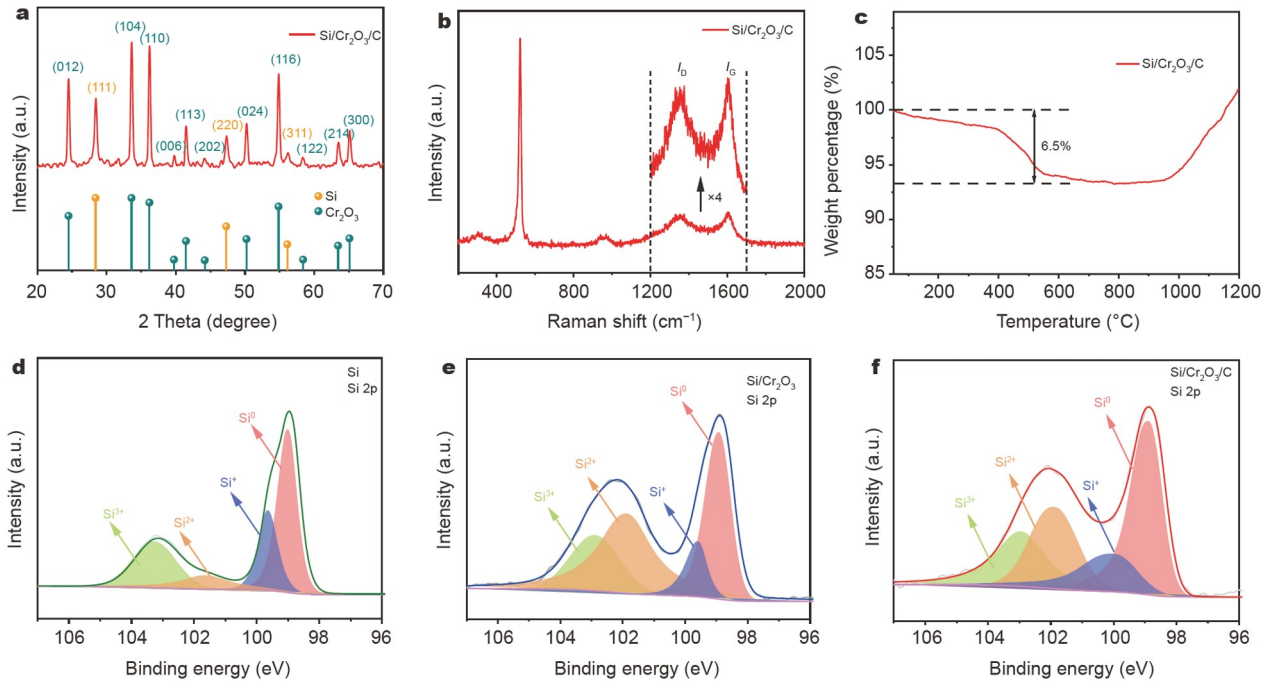

Figure 2 Structure characterizations. (a) XRD pattern of $Si/Cr_2O_3/C$; (b) Raman spectrum of $Si/Cr_2O_3/C$; (c) TGA curve of $Si/Cr_2O_3/C$; and Si 2p XPS spectra of (d) Si nanoparticles, (e) Si/Cr_2O_3, and (f) $Si/Cr_2O_3/C$.

to the alloying reaction of Si nanoparticles. In the first anodic process, the oxidation peaks at 0.34 and 0.52 V belong to the stepwise transformation from Li_xSi to amorphous Si [36]. On account of the transformation from the initial crystalline Si to amorphous Si at the end of the first charge, a peak at ~0.18 V appears in the following cathodic process, which is from the alloying process of amorphous Si. For comparison, CV profiles of the Cr_2O_3 are provided in Fig. S11. The sharp reduction peak at 0.01 V and broad oxidation peak at 1.0 V correspond to the partial reduction/re-oxidation of Cr_2O_3.

Fig. 3b presents the GCD profiles of $Si/Cr_2O_3/C$. $Si/Cr_2O_3/C$ displays a high initial discharge capacity of 1926 mA h g^{-1}. The initial Coulombic efficiencies (ICEs) of $Si/Cr_2O_3/C$ and Si/Cr_2O_3 are 64.1% and 61.4%, respectively (Fig. S12). The capacity loss can be attributed to the SEI layer formation and other irreversible reactions, which are common for Si-based anode materials [37–39]. Upon a simple pre-lithiation, the ICE of $Si/Cr_2O_3/C$ can be improved to 84.2% (Fig. S13). The long discharge plateau at ~0.15 V is from the alloying reaction of Si. This plateau is increased in the following cycles due to the reorganization of Si.

Fig. 3c compares the cycling performances. $Si/Cr_2O_3/C$ demonstrates the highest capacity among the three samples with decent cyclability. At 100 mA g^{-1}, $Si/Cr_2O_3/C$ manifests a reversible capacity of 1351 mA h g^{-1} and maintains 1007 mA h g^{-1} after 100 cycles. Si/Cr_2O_3 delivers a significantly improved capacity over Cr_2O_3/C, indicating Si nanoparticles contribute the major share of capacity despite the relatively low Si/Cr_2O_3 weight ratio (26.5% according to the feeding ratio). The further improvement in capacity for $Si/Cr_2O_3/C$ suggests that the carbon coating boosts the capacity of Si nanoparticles by enhancing electrical conductivity. Compared with bare Si nanoparticles, both $Si/Cr_2O_3/C$ and Si/Cr_2O_3 manifest significantly improved cyclability (Fig. S14), which originates from the volume buffering effect of the Cr_2O_3-based MSHS structure. Fig. 3d presents the long-term cycling performances at 500 mA g^{-1}. $Si/Cr_2O_3/C$ delivers a high reversible capacity of 1048 mA h g^{-1} and keeps a capacity of 716 mA h g^{-1} after 300 cycles. In contrast, the retained capacities for Si/Cr_2O_3 and Cr_2O_3/C are only 292 and 174 mA h g^{-1}, respectively.

The rate performances are provided in Fig. 3e and Fig. S15. For $Si/Cr_2O_3/C$, the specific capacities reach 1273, 1091, 1022, 942, and 860 mA h g^{-1} at 100, 200, 300, 500, and 1000 mA g^{-1}, respectively. Upon switching back the current density to 100 mA g^{-1}, the capacity returns to ~1060 mA h g^{-1}. For comparison, the capacities of Si/Cr_2O_3 (668 mA h g^{-1}) and Cr_2O_3/C (222 mA h g^{-1}) at 1000 mA g^{-1} are much lower than that of $Si/Cr_2O_3/C$.

EIS (Fig. S16) was conducted to compare the charge transport kinetics at the open circuit voltage (OCV) and after 50 cycles. $Si/Cr_2O_3/C$ demonstrates a smaller charge-transfer resistance (R_{ct}) value than Si/Cr_2O_3 at both states, suggesting that the carbon coating layers are imperative in enhancing electrical conductivity [40]. The improved reaction dynamics has been further confirmed by comparing Li^+ diffusion coefficients of $Si/Cr_2O_3/C$, Si/Cr_2O_3, and Si (Fig. S17) [41,42]. The Li^+ diffusion coefficient of $Si/Cr_2O_3/C$ is 2.2 times and 33.1 times higher than that of Si/Cr_2O_3 and Si, respectively. The unsatisfactory structural stability is a major limitation for high-capacity anode materials. The morphology of the active materials after cycling was studied by *ex-situ* SEM and TEM (Figs S18 and S19). The MSHS structure of $Si/Cr_2O_3/C$ is well maintained after 50 cycles, demonstrating the ideal structural integrity. In contrast, severe pulverization is observed for Si/Cr_2O_3, confirming the significant role of carbon coating in enhancing the structural integrity.

To fully evaluate the electrochemical performance of the as-synthesized materials, full-cells compromising $Si/Cr_2O_3/C$

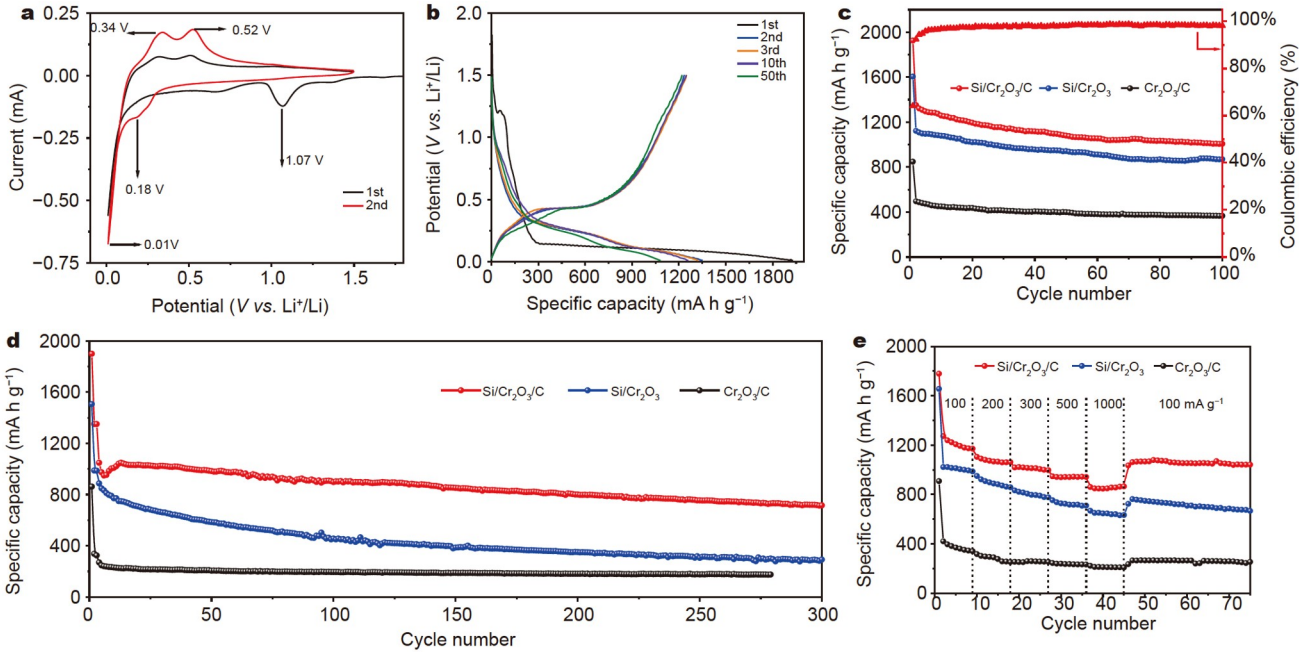

Figure 3 Electrochemical performances. (a) CV profiles and (b) representative GCD profiles of $Si/Cr_2O_3/C$; cycling performances of $Si/Cr_2O_3/C$, Si/Cr_2O_3, and Cr_2O_3/C at (c) 100 mA g^{-1} and (d) 500 mA g^{-1}; (e) rate performances of $Si/Cr_2O_3/C$, Si/Cr_2O_3, and Cr_2O_3/C. For (d), the samples are first activated at 100 mA g^{-1} for three cycles.

anodes and commercial $LiFePO_4$ cathodes were assembled. In view of the relatively low ICE, a pre-lithiation process was implemented before full-cell assembling. The $Si/Cr_2O_3/C$// $LiFePO_4$ full-cell presents an obvious discharge plateau at ~3.0 V in the GCD curves (Fig. S20a). The $Si/Cr_2O_3/C$//$LiFePO_4$ full-cell delivers a capacity of 167 mA h g^{-1} at 0.1 C based on the weight of $LiFePO_4$, which is comparable to the performance of $LiFePO_4$ in half-cells (Fig. S20b).

In-situ XRD monitors the structural evolution of $Si/Cr_2O_3/C$ during charge/discharge (Fig. 4a). The electrode at OCV shows evident characteristic peaks from both Si (28.4°) and Cr_2O_3 (33.6°, 36.2°, and 41.5°). Upon discharging, the diffraction peak for Si fades continuously, corresponding to the alloying reaction of Si. According to previous reports [43–45], the crystalline Si is transformed to amorphous phase Li_xSi at the end of initial discharging and remains amorphous in the following cycles. Meanwhile, the lithiation of Cr_2O_3 occurs and the diffractions from Cr_2O_3 weakens gradually. The lithiated product, Li_xCrO_2, appears during the first discharging and exhibits a characteristic peak at 44.1° [46]. This peak does not disappear even after recharging, suggesting the lithium ions intercalated into Cr_2O_3 cannot be completely extracted. The incomplete extraction is partially responsible for the low ICE.

In-situ Raman was further used to monitor the lithium storage process of $Si/Cr_2O_3/C$ (Fig. 4b). According to the intensity variations, two types of Raman bands can be noticed. The first type of bands at 380, 418, and 644 cm^{-1}, which can be assigned to the sapphire and electrolyte, remain constant in intensity during charge/discharge. The second type of Raman band is from Si, which is located at ~520 cm^{-1}. This band experiences periodical intensity/position changes during charge/discharge. When discharged to 0.01 V, the Raman band from Si totally disappears, which resulted from the complete alloying reaction of Si. This band does not appear during recharging, owing to the transformation from crystalline Si to an amorphous phase [47]. The *in-situ* Raman results agree perfectly with the CV and *in-situ* XRD results. As for the D-band and G-band from carbon, the intercalation of guest lithium ions into the carbonaceous host leads to the rise of disorder degree and thus affects the peak position and intensity. The decreasing intensity of the D-band upon discharging can be ascribed to the occupancy of defective sites owing to the Li^+ intercalation, thereby limiting the breathing motion of sp^2 atoms [48,49]. In addition, an inconspicuous red shift of the G-band can be observed from OCV to 0.3 V, which can be attributed to the charge transfer effects owing to lithiation and SEI layer formation [50]. The G-band almost vanishes into the signal noise at 0.01 V due to the subdued resonance from Li^+ intercalation. Generally, the position, shape, and intensity of the D- and G-bands experience a recovery during de-lithiation and change periodically during the following cycles, confirming the extraordinary reversibility of the electrode (Fig. S21).

The decent lithium storage performances of $Si/Cr_2O_3/C$ can be attributed to the following factors (Fig. 5). (1) The Si nanoparticles contribute a high capacity to the composite. (2) The MSHS structure provides additional space for accommodating the volume change of Si nanoparticles; and the porous shells provide smooth electrolyte diffusion channels. (3) The acetylene-derived carbon coating layers promote the electrical conductivity of the composite. (4) Cr_2O_3, on the one hand, contributes a certain capacity to the composite, and on the other hand, enhances the structural integrity of the composite.

CONCLUSIONS

In summary, a $Si/Cr_2O_3/C$ composite LIB anode material, where Si nanoparticles are confined in carbon-coated Cr_2O_3 multi-shell hollow microspheres, is designed. Owing to the structural merits, $Si/Cr_2O_3/C$ manifests a high reversible capacity

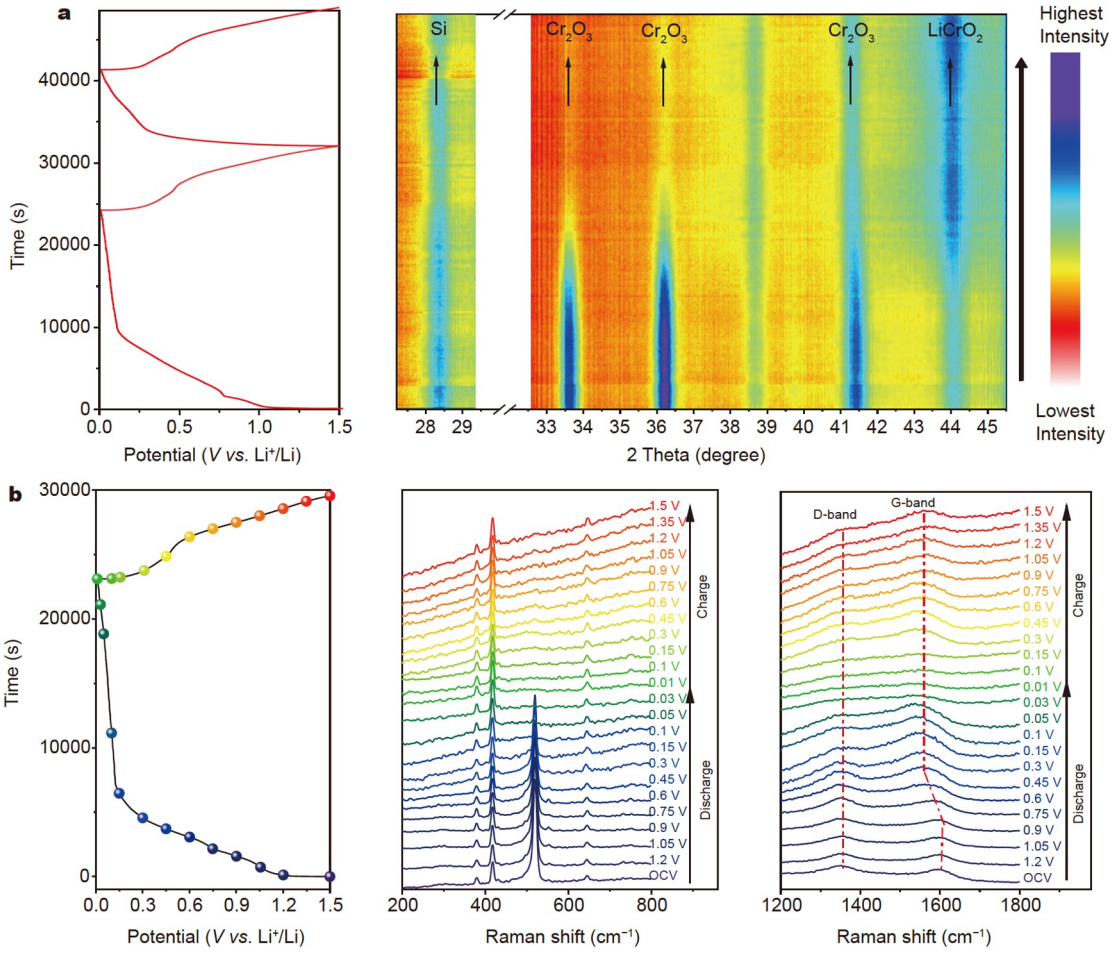

Figure 4 *In-situ* XRD and Raman characterizations. (a) *In-situ* XRD patterns of Si/Cr_2O_3/C during the first two cycles; (b) *in-situ* Raman spectra of Si/Cr_2O_3/C during the initial discharge/charge process. The current density for *in-situ* XRD and Raman testing is 100 mA g^{-1}.

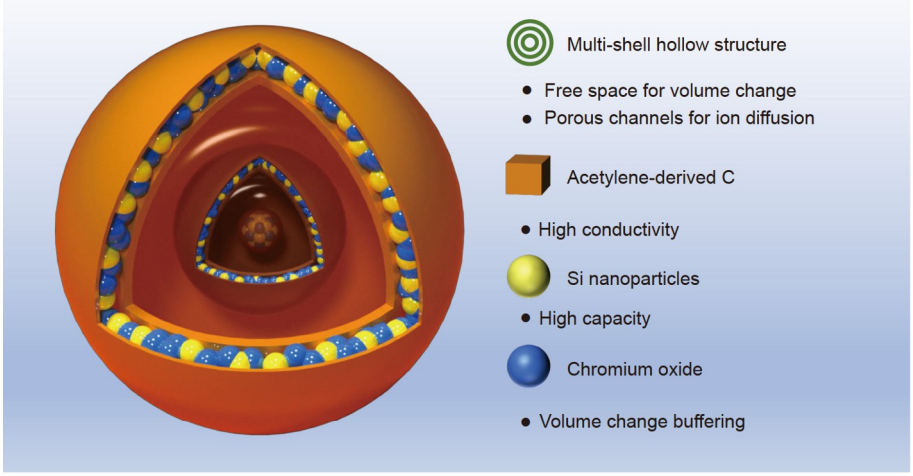

Figure 5 Schematic illustration of the Si/Cr_2O_3/C composite and the structural merits of each component.

(1351 mA h g^{-1}), satisfactory rate capability (860 mA h g^{-1} at 1000 mA g^{-1}), as well as decent cyclability (716 mA h g^{-1} after 300 cycles at 500 mA g^{-1}). This study proposes a unique MSHS structure design to handle the inherent volume expansion and conductivity problems of Si and it is promising to extend this strategy to other high-capacity anode materials.

Received 30 October 2022; accepted 20 December 2022; published online 20 March 2023

1 Pomerantseva E, Bonaccorso F, Feng X, *et al.* Energy storage: The

future enabled by nanomaterials. Science, 2019, 366: eaan8285
2 Turcheniuk K, Bondarev D, Singhal V, *et al.* Ten years left to redesign lithium-ion batteries. Nature, 2018, 559: 467–470
3 Wang Q, Liu B, Shen Y, *et al.* Confronting the challenges in lithium anodes for lithium metal batteries. Adv Sci, 2021, 8: 2101111
4 Wu F, Maier J, Yu Y. Guidelines and trends for next-generation rechargeable lithium and lithium-ion batteries. Chem Soc Rev, 2020, 49: 1569–1614
5 Lu Y, Yu L, Lou XWD. Nanostructured conversion-type anode materials for advanced lithium-ion batteries. Chem, 2018, 4: 972–996
6 Kong X, Zheng Y, Wang Y, *et al.* Necklace-like Si@C nanofibers as robust anode materials for high performance lithium ion batteries. Sci Bull, 2019, 64: 261–269
7 Zhu B, Liu G, Lv G, *et al.* Minimized lithium trapping by isovalent isomorphism for high initial Coulombic efficiency of silicon anodes. Sci Adv, 2019, 5: eaax0651
8 An W, Gao B, Mei S, *et al.* Scalable synthesis of ant-nest-like bulk porous silicon for high-performance lithium-ion battery anodes. Nat Commun, 2019, 10: 1447
9 Sun L, Liu Y, Shao R, *et al.* Recent progress and future perspective on practical silicon anode-based lithium ion batteries. Energy Storage Mater, 2022, 46: 482–502
10 Chae S, Ko M, Kim K, *et al.* Confronting issues of the practical implementation of Si anode in high-energy lithium-ion batteries. Joule, 2017, 1: 47–60
11 Chan CK, Peng H, Liu G, *et al.* High-performance lithium battery anodes using silicon nanowires. Nat Nanotech, 2008, 3: 31–35
12 Wu H, Chan G, Choi JW, *et al.* Stable cycling of double-walled silicon nanotube battery anodes through solid-electrolyte interphase control. Nat Nanotech, 2012, 7: 310–315
13 Zhang R, Du Y, Li D, *et al.* Highly reversible and large lithium storage in mesoporous Si/C nanocomposite anodes with silicon nanoparticles embedded in a carbon framework. Adv Mater, 2014, 26: 6749–6755
14 Yang J, Wang Y, Li W, *et al.* Amorphous TiO_2 shells: A vital elastic buffering layer on silicon nanoparticles for high-performance and safe lithium storage. Adv Mater, 2017, 29: 1700523
15 Liu N, Wu H, McDowell MT, *et al.* A yolk-shell design for stabilized and scalable Li-ion battery alloy anodes. Nano Lett, 2012, 12: 3315–3321
16 Magasinski A, Dixon P, Hertzberg B, *et al.* High-performance lithium-ion anodes using a hierarchical bottom-up approach. Nat Mater, 2010, 9: 353–358
17 Liu N, Lu Z, Zhao J, *et al.* A pomegranate-inspired nanoscale design for large-volume-change lithium battery anodes. Nat Nanotech, 2014, 9: 187–192
18 Wang J, Cui Y, Wang D. Hollow multishelled structures revive high energy density batteries. Nanoscale Horiz, 2020, 5: 1287–1292
19 Wang J, Wan J, Yang N, *et al.* Hollow multishell structures exercise temporal-spatial ordering and dynamic smart behaviour. Nat Rev Chem, 2020, 4: 159–168
20 Mao D, Wan J, Wang J, *et al.* Sequential templating approach: A groundbreaking strategy to create hollow multishelled structures. Adv Mater, 2019, 31: 1802874
21 Wang X, Chen Y, Fang Y, *et al.* Synthesis of cobalt sulfide multi-shelled nanoboxes with precisely controlled two to five shells for sodium-ion batteries. Angew Chem Int Ed, 2019, 58: 2675–2679
22 Yu L, Hu H, Wu HB, *et al.* Complex hollow nanostructures: Synthesis and energy-related applications. Adv Mater, 2017, 29: 1604563
23 Zhou L, Xu H, Zhang H, *et al.* Cheap and scalable synthesis of α-Fe_2O_3 multi-shelled hollow spheres as high-performance anode materials for lithium ion batteries. Chem Commun, 2013, 49: 8695–8697
24 Zhao J, Wang J, Bi R, *et al.* General synthesis of multiple-cores@multiple-shells hollow composites and their application to lithium-ion batteries. Angew Chem Intl Edit, 2021, 60: 25719–25722
25 Zhang Z, Sun S, Zhang W, *et al.* Internally inflated core-buffer-shell structural Si/EG/C composites as high-performance anodes for lithium-ion batteries. Sci China Mater, 2022, 65: 2949–2957
26 Fu S, Yu Q, Liu Z, *et al.* Yolk-shell Nb_2O_5 microspheres as intercalation pseudocapacitive anode materials for high-energy Li-ion capacitors. J Mater Chem A, 2019, 7: 11234–11240
27 Shen L, Yu L, Yu XY, *et al.* Self-templated formation of uniform $NiCo_2O_4$ hollow spheres with complex interior structures for lithium-ion batteries and supercapacitors. Angew Chem Int Ed, 2015, 54: 1868–1872
28 Guan J, Mou F, Sun Z, *et al.* Preparation of hollow spheres with controllable interior structures by heterogeneous contraction. Chem Commun, 2010, 46: 6605–6607
29 Qin J, Liu D, Zhang X, *et al.* One-step synthesis of SnCo nanoconfined in hierarchical carbon nanostructures for lithium ion battery anode. Nanoscale, 2017, 9: 15856–15864
30 Wang F, Li W, Hou M, *et al.* Sandwich-like Cr_2O_3-graphite intercalation composites as high-stability anode materials for lithium-ion batteries. J Mater Chem A, 2015, 3: 1703–1708
31 He R, Li S, Liu H, *et al.* Hetero-structured Fe-Cr-O hollow multishelled spheres for stable sodium storage. Mater Chem Front, 2022, 6: 1903–1911
32 Liu Z, Zhao Y, He R, *et al.* Yolk@shell SiO/C microspheres with semi-graphitic carbon coating on the exterior and interior surfaces for durable lithium storage. Energy Storage Mater, 2019, 19: 299–305
33 Hu G, Yu R, Liu Z, *et al.* Surface oxidation layer-mediated conformal carbon coating on Si nanoparticles for enhanced lithium storage. ACS Appl Mater Interface, 2021, 13: 3991–3998
34 Zhao L, He YB, Li C, *et al.* Compact Si/C anodes fabricated by simultaneously regulating the size and oxidation degree of Si for Li-ion batteries. J Mater Chem A, 2019, 7: 24356–24365
35 Zhao G, Wen T, Zhang J, *et al.* Two-dimensional Cr_2O_3 and interconnected grapheme-Cr_2O_3 nanosheets: Synthesis and their application in lithium storage. J Mater Chem A, 2014, 2: 944–948
36 Li H, Lu M, Han W, *et al.* Employing MXene as a matrix for loading amorphous Si generated upon lithiation towards enhanced lithium-ion storage. J Energy Chem, 2019, 38: 50–54
37 Sun L, Liu Y, Wu J, *et al.* A review on recent advances for boosting initial coulombic efficiency of silicon anodic lithium ion batteries. Small, 2022, 18: 2102894
38 He Y, Jiang L, Chen T, *et al.* Progressive growth of the solid-electrolyte interphase towards the Si anode interior causes capacity fading. Nat Nanotechnol, 2021, 16: 1113–1120
39 Kang MS, Heo I, Kim S, *et al.* High-areal-capacity of micron-sized silicon anodes in lithium-ion batteries by using wrinkled-multilayered-graphenes. Energy Storage Mater, 2022, 50: 234–242
40 Liu D, Han Z, Ma J, *et al.* Dual-confined SiO encapsulated in PVA derived carbon layer and chitin derived N-doped carbon nanosheets for high-performance lithium storage. Chem Eng J, 2021, 420: 129754
41 Xu C, Xia T, Wang C, *et al.* Stable and fast Si-M-C ternary anodes enabled by interfacial engineering. J Power Sources, 2022, 530: 231290
42 Xu C, Xia T, Li X, *et al.* Covalent binding of holey Si-SiC layer on graphene aerogel with enhanced lithium storage kinetics and capability. Surf Coatings Tech, 2021, 420: 127336
43 Bärmann P, Mohrhardt M, Frerichs JE, *et al.* Mechanistic insights into the pre-lithiation of silicon/graphite negative electrodes in “dry state” and after electrolyte addition using passivated lithium metal powder. Adv Energy Mater, 2021, 11: 2100925
44 Kitada K, Pecher O, Magusin PCMM, *et al.* Unraveling the reaction mechanisms of SiO anodes for Li-ion batteries by combining *in situ* ^{7}Li and *ex situ* ^{7}Li/^{29}Si solid-state NMR spectroscopy. J Am Chem Soc, 2019, 141: 7014–7027
45 Loaiza LC, Monconduit L, Seznec V. Si and Ge-based anode materials for Li-, Na-, and K-ion batteries: A perspective from structure to electrochemical mechanism. Small, 2020, 16: 1905260
46 Fister TT, Hu X, Esbenshade J, *et al.* Dimensionally controlled lithiation of chromium oxide. Chem Mater, 2016, 28: 47–54
47 Zeng Z, Liu N, Zeng Q, *et al. In situ* measurement of lithiation-induced stress in silicon nanoparticles using micro-Raman spectroscopy. Nano Energy, 2016, 22: 105–110
48 Qian Y, Jiang S, Li Y, *et al. In situ* revealing the electroactivity of P-O and P-C bonds in hard carbon for high-capacity and long-life Li/K-ion batteries. Adv Energy Mater, 2019, 9: 1901676
49 Oh YJ, Park JH, Park JS, *et al.* Fast-chargeable N-doped multi-oriented

graphitic carbon as a Li-intercalation compound. Energy Storage Mater, 2022, 44: 416–424
50 Sbrascini L, Staffolani A, Bottoni L, *et al.* Structural and interfacial characterization of a sustainable Si/hard carbon composite anode for lithium-ion batteries. ACS Appl Mater Interface, 2022, 14: 33257–33273

Acknowledgements This work was supported by the Key Research and Development Program of Hubei Province (2021BAA176) and Hainan Provincial Natural Science Foundation of China (522CXTD516). The S/TEM was performed at the Nanostructure Research Center (NRC), Wuhan University of Technology.

Author contributions Du H and Zhou L conceived the idea, planned the study, and participated in the data analysis. Du H carried out the materials synthesis and the electrochemical evaluation as well as wrote the manuscript. Yu R and Tan X helped with materials characterizations and schematic diagram plots. Wu J provided insights for the experiments and supervised the research. Zhou L, Zhao D, and Mai L contributed to the conception of the study and revised the manuscript. All the authors discussed the results and commented on the manuscript.

Conflict of interest The authors declare that they have no conflict of interest.

Supplementary information Supporting data are available in the online version of the paper.

Huan Du received his BS degree from the International School of Materials Science and Engineering (ISMSE), Wuhan University of Technology. He is currently an MS candidate at Wuhan University of Technology. His research focuses on developing novel nanomaterials for lithium-ion batteries.

Liang Zhou received his PhD degree from the Department of Chemistry, Fudan University in 2011. After graduation, he worked as a postdoctoral research fellow at Nanyang Technological University (2011–2012) and The University of Queensland (2012–2015). He is now a full professor at Wuhan University of Technology. His research interest includes functional nanomaterials for electrochemical energy storage.

将硅纳米颗粒限域在多壳层空心球: 一种提升循环稳定性的有效策略

杜寰[1,2], 余若翰[2,3], 谭兴念[1], 吴劲松[1,3], 赵东元[1], 麦立强[1,4], 周亮[1,4*]

摘要 单质硅是一种有潜力的高容量锂离子电池负极材料. 然而, 受限于充放电过程中巨大的体积膨胀, 其循环性能并不理想. 在这个工作中, 我们设计了一种独特的三组分复合负极材料(Si/Cr_2O_3/C), 其中Si纳米颗粒被限域在碳包覆的氧化铬多层空心球(MSHSs)中. 得益于Cr_2O_3/C基体的体积变化缓冲能力与优异的结构稳定性, 将Si纳米颗粒封装在MSHSs中可以有效地提高其电化学性能. 合理的结构设计赋予了Si/Cr_2O_3/C三组分复合材料高的可逆容量(在100 mA g^{-1}的电流密度下, 比容量为1351 mA h g^{-1})和稳定的循环性能(在500 mA g^{-1}的电流密度下, 循环300次后比容量保持在716 mA h g^{-1}). 这一工作提出了一种多壳层空心结构设计的新思路, 以解决硅基负极材料循环性差的瓶颈.